

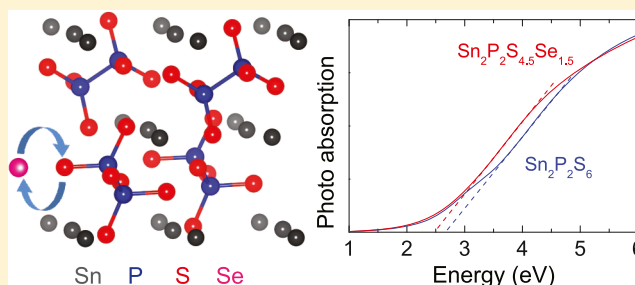
# Enhancing Visible Light Absorption for Ferroelectric $\text{Sn}_2\text{P}_2\text{S}_6$ by Se Anion Substitution

Min Zhao, Gaoyang Gou,\*<sup>✉</sup> Xiangdong Ding, and Jun Sun

Frontier Institute of Science and Technology, and State Key Laboratory for Mechanical Behavior of Materials, Xi'an Jiaotong University, Xi'an 710049, People's Republic of China

## Supporting Information

**ABSTRACT:** Ferroelectric (FE) semiconductors that simultaneously exhibit spectrally suitable band gaps and room temperature stable FE polarizations necessary for separation of photo-excited carriers have been extensively investigated for FE-photovoltaic (PV) applications. Di tin hexathiohypodiphosphate,  $\text{Sn}_2\text{P}_2\text{S}_6$ , is one of the rare semiconducting FE materials. However, owing to the indirect nature of its energy band gap and relatively large direct band gap, FE  $\text{Sn}_2\text{P}_2\text{S}_6$  absorbs only a small portion of the visible light spectrum. In the current work, we propose substitution of S by Se anion as an experimental feasible route to enhance the visible light absorption for FE  $\text{Sn}_2\text{P}_2\text{S}_6$ . Using first-principles calculations, we demonstrate that the effective “band gap engineering” with respect to Se substitution concentration can be achieved in  $\text{Sn}_2\text{P}_2\text{S}_{6(1-x)}\text{Se}_{6x}$  solid solutions. Especially,  $\text{Sn}_2\text{P}_2\text{S}_{4.5}\text{Se}_{1.5}$  compound is predicted to be an indirect band gap semiconductor, with a direct band gap at  $\Gamma$  point even lower than that of  $\text{BiFeO}_3$ , and meanwhile exhibits a stable ferroelectricity comparable with single-phase  $\text{Sn}_2\text{P}_2\text{S}_6$ . As a result, the improved visible light absorption can be achieved in  $\text{Sn}_2\text{P}_2\text{S}_{4.5}\text{Se}_{1.5}$  compound, making Se-doped FE  $\text{Sn}_2\text{P}_2\text{S}_6$  more suitable for PV applications.



## INTRODUCTION

Solar energy conversion through the photovoltaic (PV) effect requires the efficient absorption of visible light as well as effective separation of photo-excited electron–hole pairs. Traditional PV devices are based on semiconductor p–n junctions, which rely on the potential difference across the p–n junction to separate the carrier pairs. On the other hand, ferroelectric (FE) materials with spontaneous polarizations are promising PV alternatives. As the incident sun light is absorbed by a single-phase FE material, photo-excited carriers can be effectively separated by the built-in electric field, leading to the novel FE-PV effect.<sup>1,2</sup> Moreover, the photo current and voltage generated through FE-PV effect can be switched by the applied electric field.<sup>3–5</sup> As a result, the electric switchable PV response enables the electric-writing and optical-reading memory operations in FE-PV devices.<sup>6</sup>

FE  $\text{BiFeO}_3$ <sup>7–10</sup> and its derivatives (e.g., double perovskite  $\text{Bi}_2\text{FeCrO}_6$ <sup>11,12</sup>) have been extensively investigated for FE-PV applications. Unlike the common FE perovskite oxides, which are wide-gap insulators ( $E_g > 3.0$  eV),<sup>13</sup>  $\text{BiFeO}_3$  has an energy band gap ( $E_g = 2.67$  eV)<sup>14</sup> within the visible light energy range, able to absorb a portion of visible spectrum. Besides  $\text{BiFeO}_3$ , many other FE semiconductors have been proposed for PV applications.<sup>15–20</sup> For example, we designed Ruddlesden–Popper  $\text{Ca}_3\text{Zr}_2\text{S}_7$  as a FE perovskite sulfide for solar energy conversion.<sup>21</sup> As most sulfides are semiconductors with smaller  $E_g$  than insulating perovskite oxides, sulfide compounds are more suitable for visible light absorption. However, perovskite

sulfide  $\text{Ca}_3\text{Zr}_2\text{S}_7$  with Ruddlesden–Popper layered structure requires the unique thin-film growth technique, making it hard for massive production of  $\text{Ca}_3\text{Zr}_2\text{S}_7$  for practical FE-PV applications.

As a matter of fact, di tin hypthiodiphosphate,  $\text{Sn}_2\text{P}_2\text{S}_6$ , a rare FE sulfide with non-perovskite structure, has been synthesized in experiment. Typically,  $\text{Sn}_2\text{P}_2\text{S}_6$  single crystals can be prepared using a chemical vapor transfer technique,<sup>22–26</sup> whereas its ceramic samples were obtained through solid-state sintering process.<sup>23,27</sup> As-grown  $\text{Sn}_2\text{P}_2\text{S}_6$  samples show good stability against moisture and oxygen oxidation at ambient condition.<sup>28</sup> Moreover,  $\text{Sn}_2\text{P}_2\text{S}_6$  exhibits room temperature stable ferroelectricity, which can be directly measured in experiment.<sup>23,27,29</sup> Optical spectrum measurement demonstrates  $\text{Sn}_2\text{P}_2\text{S}_6$  as a semiconductor with relatively narrow band gap.<sup>24</sup> However, the indirect nature of the energy band gap and relatively large direct band gap of  $\text{Sn}_2\text{P}_2\text{S}_6$  make it less effective for visible light absorption.<sup>24</sup> Therefore, identifying practical ways to modify the energy band gap and enhance the visible light absorption is required for development of  $\text{Sn}_2\text{P}_2\text{S}_6$ -based FE-PV materials. Recently, first principles calculations performed by Li et al.<sup>30</sup> indicate that FE  $\text{Sn}_2\text{P}_2\text{Se}_6$  with a lower band gap ( $E_g \approx 1.8$  eV) are more suitable as solar absorbing material than  $\text{Sn}_2\text{P}_2\text{S}_6$ . However, the

Received: August 29, 2018

Revised: October 15, 2018

Published: October 16, 2018



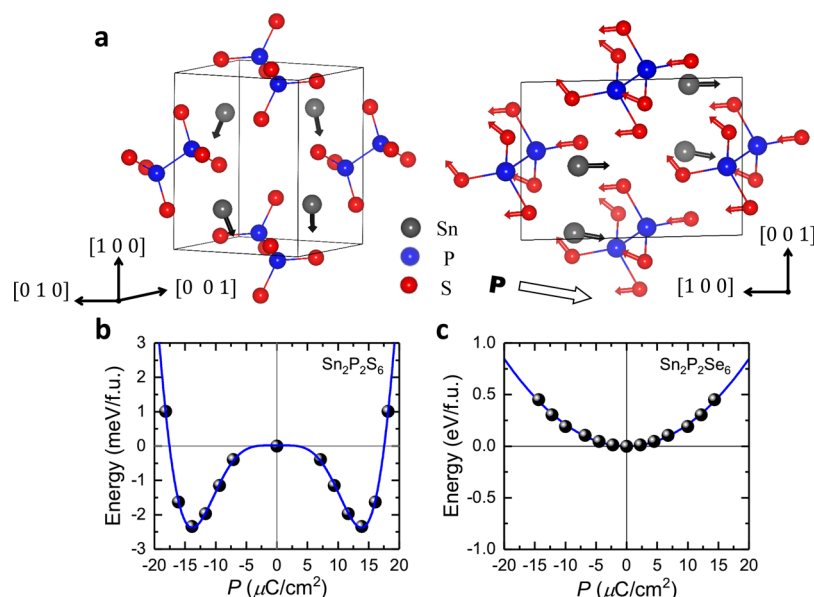


**Figure 1.** (a) Major atomic displacement (indicated by arrows) of FE  $Pc$   $\text{Sn}_2\text{P}_2\text{S}_6$  phase with respect to the paraelectric  $P2_1/c$  phase. Both top view and side view (projected along  $[101]$  plane) are presented. Sn, P, and S atoms are in gray, blue, and red, respectively. For clarity, polar displacements of S atoms are shown only in the side view plot. Evolution of total energy with amplitude of polar displacement relative to paraelectric phase for (b)  $\text{Sn}_2\text{P}_2\text{S}_6$  and (c)  $\text{Sn}_2\text{P}_2\text{Se}_6$ . Symbols are first-principles results and lines are fitted based on Landau phenomenological model. Double-well polarization energy curve indicates that  $\text{Sn}_2\text{P}_2\text{S}_6$  has a FE phase as its stable structure. However,  $P2_1/c$  paraelectric phase is a vibrational stable and a low-lying ground-state structure for single-phase  $\text{Sn}_2\text{P}_2\text{Se}_6$ .

presence of ferroelectricity in single-phase  $\text{Sn}_2\text{P}_2\text{Se}_6$  is still under debate, as experimental  $\text{Sn}_2\text{P}_2\text{Se}_6$  samples always exhibit the incommensurate phases.<sup>22,23,31</sup> On the other hand, isovalent anion substitution (e.g., substitution of O by S, S by Se) has been proven as an effective band gap engineering approach for many semiconductor materials.<sup>2,32–34</sup> Selenide  $\text{Sn}_2\text{P}_2\text{Se}_6$  possesses non-perovskite structure similar to  $\text{Sn}_2\text{P}_2\text{S}_6$ .<sup>22</sup> Owing to the good solubility between S and Se anions, stoichiometric  $\text{Sn}_2\text{P}_2\text{S}_{6(1-x)}\text{Se}_{6x}$  solid solutions can be created after alloying  $\text{Sn}_2\text{P}_2\text{S}_6$  and  $\text{Sn}_2\text{P}_2\text{Se}_6$ . In fact,  $\text{Sn}_2\text{P}_2\text{S}_{6(1-x)}\text{Se}_{6x}$  single crystals have been successfully prepared using either vapor transport or Bridgman technique.<sup>35,36</sup> Once  $\text{Sn}_2\text{P}_2\text{S}_{6(1-x)}\text{Se}_{6x}$  compounds simultaneously exhibit stable ferroelectricity and spectrally more suitable band gaps, they can be promising alternatives to single-phase  $\text{Sn}_2\text{P}_2\text{S}_6$  for FE-PV applications.

In this work, we use first-principles calculations to investigate the effect of Se substitution on FE, electronic, and optical absorption properties for single-phase  $\text{Sn}_2\text{P}_2\text{S}_6$ . We first identify the ground-state crystal structures for  $\text{Sn}_2\text{P}_2\text{S}_6$  and  $\text{Sn}_2\text{P}_2\text{Se}_6$ , using the systematic structure analysis and optimization scheme. After isovalent and isomorphous substitution of S anions by Se,  $\text{Sn}_2\text{P}_2\text{S}_{6(1-x)}\text{Se}_{6x}$  solid solutions with low Se concentration ( $x \leq 25\%$ ) are predicted to exhibit stable ferroelectricity comparable with that of  $\text{Sn}_2\text{P}_2\text{S}_6$ . Detailed crystal structure analysis is also performed to rationalize the simulated FE properties. Moreover, the effective reduction of band gaps in  $\text{Sn}_2\text{P}_2\text{S}_{6(1-x)}\text{Se}_{6x}$  with respect to Se concentration is obtained, leading to improved visible light absorption of  $\text{Sn}_2\text{P}_2\text{S}_{6(1-x)}\text{Se}_{6x}$  over the single-phase  $\text{Sn}_2\text{P}_2\text{S}_6$ .

## COMPUTATIONAL METHODS

Our first-principles calculations are performed within density functional theory implemented in the Vienna Ab Initio Simulation Package (VASP),<sup>37,38</sup> using projector augmented

wave pseudopotentials<sup>39</sup> and a plane wave basis set with energy cutoff of 500 eV. PBEsol functional<sup>40</sup> is chosen for structural optimization, as it can provide the improved structural results over LDA or GGA-PBE.<sup>41</sup> Single-phase  $\text{Sn}_2\text{P}_2\text{S}_6$  ( $\text{Sn}_2\text{P}_2\text{Se}_6$ ) crystallizes in a monoclinic phase, containing 20 atoms in its primary unit cell (see Figure 1).  $\text{Sn}_2\text{P}_2\text{S}_{6(1-x)}\text{Se}_{6x}$  solid solutions are simulated using a 40-atom supercell, which is obtained by doubling the  $\text{Sn}_2\text{P}_2\text{S}_6$  unit cell along the diagonal directions ( $1 \times \sqrt{2} \times \sqrt{2}$  repetition of  $\text{Sn}_2\text{P}_2\text{S}_6$  unit cell).  $4 \times 6 \times 6$  and  $4 \times 4 \times 4$  Monkhorst–Pack  $k$ -point grids<sup>42</sup> are used to sample the Brillouin zone for single-phase  $\text{Sn}_2\text{P}_2\text{S}_6$  ( $\text{Sn}_2\text{P}_2\text{Se}_6$ ) and  $\text{Sn}_2\text{P}_2\text{S}_{6(1-x)}\text{Se}_{6x}$  solid solutions, respectively. All structures are fully relaxed until the Hellmann–Feynman force on each atom is less than 0.1 meV/Å and stress less than 0.1 kbar. Following the structural optimization, we further calculate the electronic structures and optical absorption properties of optimized chalcogenide compounds using Heyd–Scuseria–Ernzerhof (HSE06)<sup>43</sup> hybrid functional. Spin-orbital coupling (SOC) is excluded in HSE calculations, as band gap changes arising from SOC effect in single-phase  $\text{Sn}_2\text{P}_2\text{S}_6$  and  $\text{Sn}_2\text{P}_2\text{Se}_6$  are quite small.<sup>30</sup> Phonon frequencies and eigenvectors are simulated based on density functional perturbation theory (DFPT).<sup>44,45</sup> Electronic contribution to the polarization is calculated following the Berry phase formalism.<sup>46</sup>

## RESULTS AND DISCUSSION

**Structural and FE Properties.** *Single-Phase  $\text{Sn}_2\text{P}_2\text{S}_6$  and  $\text{Sn}_2\text{P}_2\text{Se}_6$ .* Both  $\text{Sn}_2\text{P}_2\text{S}_6$  and  $\text{Sn}_2\text{P}_2\text{Se}_6$  belong to transition metal phosphorus chalcogenide family with the chemical formula  $\text{M}_2\text{P}_2\text{X}_6$  ( $\text{M} = \text{Sn, Pb}$  and  $\text{X} = \text{S, Se}$ ). In their primary unit cells,  $\text{Sn}_2\text{P}_2\text{S}_6$  and  $\text{Sn}_2\text{P}_2\text{Se}_6$  contain two  $(\text{P}_2\text{X}_6)^{4-}$  anionic units, whereas four  $\text{Sn}^{2+}$  cations are arranged between these anionic units<sup>28</sup> (Figure 1). Each  $(\text{P}_2\text{X}_6)^{4-}$  unit consists of two distorted trigonal  $\text{PX}_3$  pyramids bound by a P–P bond. In

**Table 1.** Comparison between the Experimental and Our Calculated Lattice Parameters; FE Polarization,  $P$ ; and Energy band Gaps,  $E_g$ , for Single-Phase  $\text{Sn}_2\text{P}_2\text{S}_6$  and  $\text{Sn}_2\text{P}_2\text{Se}_6$ <sup>a</sup>

		$a$ (Å)	$b$ (Å)	$c$ (Å)	$\beta$ (deg)	$P$ ( $\mu\text{C}/\text{cm}^2$ )	$E_g$ (eV)
FE $\text{Sn}_2\text{P}_2\text{S}_6$	exp. <sup>48</sup>	9.378	7.488	6.513	91.15	14.0 <sup>23,29</sup>	2.3 <sup>25,49</sup>
	cal.	9.183	7.440	6.495	91.24	13.9	2.23(2.79)
paraelectric $\text{Sn}_2\text{P}_2\text{S}_6$	exp. <sup>50</sup>	9.362	7.493	6.550	91.17		
	cal.	9.110	7.425	6.493	91.32		
paraelectric $\text{Sn}_2\text{P}_2\text{Se}_6$	exp. <sup>51</sup>	9.587	7.682	6.808	90.94		
	cal.	9.438	7.641	6.852	91.60		1.80(2.22)

<sup>a</sup>The calculated direct band gaps at  $\Gamma$  point for single-phase  $\text{Sn}_2\text{P}_2\text{S}_6$  and  $\text{Sn}_2\text{P}_2\text{Se}_6$  are given in parentheses.

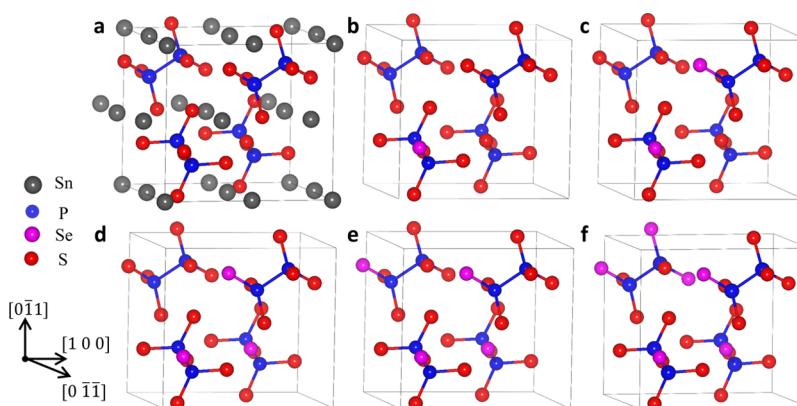


**Figure 2.** (a) Supercell configuration composed of  $1 \times \sqrt{2} \times \sqrt{2}$   $\text{Sn}_2\text{P}_2\text{S}_6$  primary cell is used for simulation of  $\text{Sn}_2\text{P}_2\text{S}_6(1-x)\text{Se}_{6x}$  solid solutions. (b–f) The most energetic stable  $\text{Sn}_2\text{P}_2\text{S}_6(1-x)\text{Se}_{6x}$  configurations with Se concentration  $x = 4.2, 8.3, 12.5, 16.7$ , and  $25\%$ . The major component of FE polarization is directed along the  $[100]$  direction of the supercell configuration. Sn, Se, P, and S atoms are marked in dark gray, pink, blue, and red, respectively. Sn atoms are omitted for clarity in (b–f).

experiment, single-phase  $\text{Sn}_2\text{P}_2\text{S}_6$  crystallizes in a polar space group  $Pc$  (no. 7) with monoclinic symmetry and displays a moderate FE polarization along the  $[101]$  direction.<sup>27</sup> Above Curie temperature ( $T_C = 339$  K), it transforms into a centrosymmetric paraelectric monoclinic phase (space group  $P2_1/c$ , no. 14).<sup>22,27</sup> Unlike the displacive structural transition in  $\text{Sn}_2\text{P}_2\text{S}_6$ ,  $\text{Sn}_2\text{P}_2\text{Se}_6$  undergoes two order–disorder-type phase transitions at 193 and 220 K, respectively, resulting in intermediate incommensurate structural phases.<sup>22,31</sup> Owing to the order–disorder nature of its structural transition and the presence of incommensurate phases, it is hard to precisely determine the low-temperature ground-state crystal structure for ordered  $\text{Sn}_2\text{P}_2\text{Se}_6$ . Only high-temperature  $P2_1/c$  paraelectric  $\text{Sn}_2\text{P}_2\text{Se}_6$  phase is available in experiment.<sup>23</sup>

We determine the ground-state structures for single-phase  $\text{Sn}_2\text{P}_2\text{S}_6$  and  $\text{Sn}_2\text{P}_2\text{Se}_6$  as follows: we choose the experimentally available centrosymmetric  $P2_1/c$  phase as paraelectric reference, from which the unstable phonon modes and the associated structure instabilities can be obtained from DFPT calculations. For  $\text{Sn}_2\text{P}_2\text{S}_6$ , paraelectric phase with  $P2_1/c$  symmetry has an unstable polar mode with imaginary frequency ( $\omega = i\ 20.5\ \text{cm}^{-1}$ ), corresponding to the polar displacement of Sn cations along the  $[101]$  direction.<sup>47</sup> After freezing the unstable polar mode into the  $P2_1/c$  phase, followed by structural optimization, polar  $Pc$  phase with non-zero FE polarization is obtained for  $\text{Sn}_2\text{P}_2\text{S}_6$ . Further DFPT calculation confirms FE  $Pc$  phase as the vibrationally stable and ground-state structure for  $\text{Sn}_2\text{P}_2\text{S}_6$ . Tables 1 and S1 of the Supporting Information summarize our calculated crystallographic parameters for FE and paraelectric  $\text{Sn}_2\text{P}_2\text{S}_6$  phases, both in good agreement with experimental measurement.

In addition, Berry phase calculation predicts a spontaneous polarization of  $13.9\ \mu\text{C}/\text{cm}^2$  for FE  $\text{Sn}_2\text{P}_2\text{S}_6$ , very close to experimentally measured value ( $P \approx 14.0\ \mu\text{C}/\text{cm}^2$ ).<sup>23,29</sup> In order to understand the FE mechanism of  $\text{Sn}_2\text{P}_2\text{S}_6$ , we examine the atomic displacement and the energy profile connecting the paraelectric  $P2_1/c$  and FE  $Pc$  phases. As shown in Figure 1a, polar displacement of Sn cations opposite to S anions can break inversion symmetry of paraelectric  $\text{Sn}_2\text{P}_2\text{S}_6$  phase and create a net FE polarization along the crystallographic  $[101]$  direction (major polarization component is along the  $[100]$  direction). After recording the variation of the FE polarization and total energy of  $\text{Sn}_2\text{P}_2\text{S}_6$  with respect to the polar displacement connecting its paraelectric and FE phases, a typical double-well polarization–energy curve is obtained (Figure 1b). Such a  $P$ – $E$  curve can be well fitted using a second-order (continuous) Landau–Devonshire phenomenological model as:  $E = \alpha/2(T - T_C) \times P^2 + \beta/4 \times P^4$  (blue line in Figure 1b), where  $\alpha$  and  $\beta$  are positive parameters and  $T_C$  is Curie temperature of  $\text{Sn}_2\text{P}_2\text{S}_6$ . Here we estimate  $T_C$  using the Abrahams relation:  $T_C = (2.0 \times 10^4) \times (\Delta z)^2$  K, where  $\Delta z$  is the largest cation displacement along the polarization direction, after a shift of origin to make  $\sum \Delta z = 0$ .<sup>52</sup> For ferroelectric  $\text{Sn}_2\text{P}_2\text{S}_6$ ,  $\Delta z = \pm 0.14\ \text{\AA}$  for Sn and P ions, respectively. As a result, the estimated  $T_C$  is 392 K, close to the experimental value ( $T_C = 339$  K).<sup>22</sup> Therefore,  $\text{Sn}_2\text{P}_2\text{S}_6$  is a proper FE material similar to perovskite  $\text{BaTiO}_3$  or  $\text{PbTiO}_3$ , whose FE polarization is mainly contributed by ion polar displacement.

Following the same procedure, we also perform structural optimization for single-phase  $\text{Sn}_2\text{P}_2\text{Se}_6$ . Our DFPT calculations indicate that paraelectric  $\text{Sn}_2\text{P}_2\text{Se}_6$  phase with  $P2_1/c$  symmetry (crystallographic parameters given in Tables 1 and S1) is



vibrationally stable and free of any polar instability. If we displace the atomic coordinates of  $\text{Sn}_2\text{P}_2\text{S}_6$  based on the polar displacement pattern found in  $\text{Sn}_2\text{P}_2\text{S}_6$ , a single-well  $P$ – $E$  curve, where the paraelectric phase is located at the energy minimum, will be obtained (Figure 1c, with Landau energy expansion as:  $E = A/2 \times P^2$ ,  $A > 0$ ). We can therefore conclude that single-phase  $\text{Sn}_2\text{P}_2\text{S}_6$  has paraelectric  $P2_1/c$  phase as its ground-state stable structure, without any detectable FE polarization. However, it is noted that the aforementioned conclusion is based on the calculations performed on the periodic and commensurate  $\text{Sn}_2\text{P}_2\text{S}_6$  system. Owing to the fact that there exist incommensurate structural phases in experimental  $\text{Sn}_2\text{P}_2\text{S}_6$  samples, the presence of ferroelectricity in incommensurate  $\text{Sn}_2\text{P}_2\text{S}_6$  phase cannot be excluded.<sup>31</sup>

**$\text{Sn}_2\text{P}_2\text{S}_{6(1-x)}\text{Se}_{6x}$  Solid Solution.** Single-phase  $\text{Sn}_2\text{P}_2\text{S}_6$  and  $\text{Sn}_2\text{P}_2\text{Se}_6$  are stoichiometric compounds with similar crystallographic symmetry. Owing to the isostructural nature of their crystal structures and similar ionic radii between S and Se anions (1.84 vs 1.98 Å),  $\text{Sn}_2\text{P}_2\text{S}_6$  and  $\text{Sn}_2\text{P}_2\text{Se}_6$  can be used as two end-member compounds for  $\text{Sn}_2\text{P}_2\text{S}_{6(1-x)}\text{Se}_{6x}$  solid solutions. More importantly, after isovalent and isomorphous substitution of S anions by Se,  $\text{Sn}_2\text{P}_2\text{S}_{6(1-x)}\text{Se}_{6x}$  solid solution can maintain a crystal structure similar to  $\text{Sn}_2\text{P}_2\text{S}_6$ , without any nonstoichiometric defects or vacancies. In this subsection, structural and FE properties of  $\text{Sn}_2\text{P}_2\text{S}_{6(1-x)}\text{Se}_{6x}$  will be examined.

Figure 2a displays a 40-atom supercell we constructed for simulation of  $\text{Sn}_2\text{P}_2\text{S}_{6(1-x)}\text{Se}_{6x}$  solid solutions. Such a supercell is large enough to capture the ion polar displacement and Se doping induced structural disorder in  $\text{Sn}_2\text{P}_2\text{S}_{6(1-x)}\text{Se}_{6x}$  systems.<sup>53</sup> Further expansion of supercell size does not lead to obvious change in the simulated energetic, structural, and FE results for  $\text{Sn}_2\text{P}_2\text{S}_{6(1-x)}\text{Se}_{6x}$  (Figure S1 of the Supporting Information). In experimental  $\text{Sn}_2\text{P}_2\text{S}_{6(1-x)}\text{Se}_{6x}$  samples, incommensurate structural phases emerge when Se concentration  $x$  is larger than 28%.<sup>36,54</sup> To simulate those periodic and commensurate  $\text{Sn}_2\text{P}_2\text{S}_{6(1-x)}\text{Se}_{6x}$  structures, we choose to replace 1, 2, 3, 4, and 6 S atoms by Se, corresponding to a series of  $\text{Sn}_2\text{P}_2\text{S}_{6(1-x)}\text{Se}_{6x}$  solid solutions with maximal Se concentration  $x = 25\%$ . For  $\text{Sn}_2\text{P}_2\text{S}_{6(1-x)}\text{Se}_{6x}$  configuration containing more than one Se atom, we consider all possible arrangements between Se anions to evaluate the anion substitution-induced structural disorder effect. After structural optimization, we double check the stability of each  $\text{Sn}_2\text{P}_2\text{S}_{6(1-x)}\text{Se}_{6x}$  configuration against the random atomic and cell distortions, so that our optimized  $\text{Sn}_2\text{P}_2\text{S}_{6(1-x)}\text{Se}_{6x}$  configurations are confirmed to be energy minima. In this way, each stable  $\text{Sn}_2\text{P}_2\text{S}_{6(1-x)}\text{Se}_{6x}$  configuration we simulated can be considered as a local structural snapshot of the experimental solid solutions.

To evaluate thermodynamic stabilities of  $\text{Sn}_2\text{P}_2\text{S}_{6(1-x)}\text{Se}_{6x}$  configurations, we calculate their solution energies, corresponding to the energy gain for alloying single-phase  $\text{Sn}_2\text{P}_2\text{S}_6$  and  $\text{Sn}_2\text{P}_2\text{Se}_6$  into  $\text{Sn}_2\text{P}_2\text{S}_{6(1-x)}\text{Se}_{6x}$  solid solutions:  $\Delta E = E[\text{Sn}_2\text{P}_2\text{S}_{6(1-x)}\text{Se}_{6x}] - (1 - x) \times E[\text{Sn}_2\text{P}_2\text{S}_6] - x \times E[\text{Sn}_2\text{P}_2\text{Se}_6]$ , where  $E[\text{Sn}_2\text{P}_2\text{S}_6]$  and  $E[\text{Sn}_2\text{P}_2\text{Se}_6]$  are normalized energy for single-phase FE  $\text{Sn}_2\text{P}_2\text{S}_6$  and paraelectric  $\text{Sn}_2\text{P}_2\text{Se}_6$  respectively. The negative value of  $\Delta E$  means  $\text{Sn}_2\text{P}_2\text{S}_{6(1-x)}\text{Se}_{6x}$  configuration meets the thermodynamic stable condition, without decomposition into separated  $\text{Sn}_2\text{P}_2\text{S}_6$  and  $\text{Sn}_2\text{P}_2\text{Se}_6$  compounds. Atomic structures of all stable  $\text{Sn}_2\text{P}_2\text{S}_{6(1-x)}\text{Se}_{6x}$  configurations ( $\Delta E < 0$ ) we simulated are tabulated in Figure S2 of the Supporting Information. Among

those configurations, the most energetic stable  $\text{Sn}_2\text{P}_2\text{S}_{6(1-x)}\text{Se}_{6x}$  structures under different Se concentrations are displayed in Figure 2b–f. Using the simulated  $\text{Sn}_2\text{P}_2\text{S}_{6(1-x)}\text{Se}_{6x}$  configurations, we can examine how energetic stability of  $\text{Sn}_2\text{P}_2\text{S}_{6(1-x)}\text{Se}_{6x}$  varies as a function of Se concentrations. Figure 3a shows the evolution of the solution energy of

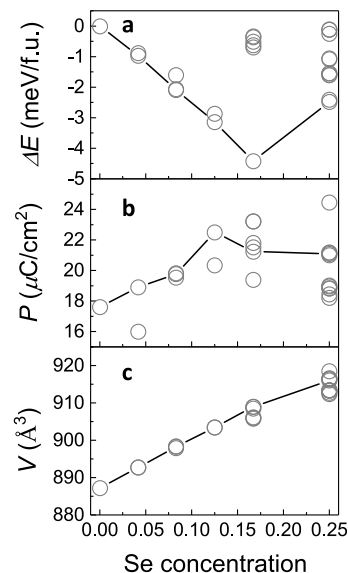


**Figure 3.** Variation of (a) solution energy  $\Delta E$ , (b) spontaneous polarization  $P$ , and (c) the cell volume  $V$  (per 40-atom supercell) for stable  $\text{Sn}_2\text{P}_2\text{S}_{6(1-x)}\text{Se}_{6x}$  configurations as a function of Se concentration  $x$ . The results corresponding to the most energetic stable configurations under different Se concentrations are connected by solid lines.

$\text{Sn}_2\text{P}_2\text{S}_{6(1-x)}\text{Se}_{6x}$  configurations with respect to Se concentration, where the minimal solution energy ( $\Delta E \approx -4.5$  meV/f.u.) occurs at the Se concentration  $x = 16.7\%$ . Under this concentration, the relatively large energy difference between the most stable and other low-lying configurations indicates that it is likely to prepare  $\text{Sn}_2\text{P}_2\text{S}_5\text{Se}$  sample with ordered S/Se anion arrangement. Besides energetic stability, we also verify the dynamic and vibrational stability of the system. We compute the phonon spectrum of the most stable  $\text{Sn}_2\text{P}_2\text{S}_{4.5}\text{Se}_{1.5}$  configuration (Se concentration  $x = 25\%$ ) using DFPT method. It is found that such a configuration is vibrationally stable and free of structural instabilities (Figure S3).

The evolution of FE properties of  $\text{Sn}_2\text{P}_2\text{S}_{6(1-x)}\text{Se}_{6x}$  solid solution with respect to Se concentration is examined next. Figure 3b,c display our calculated FE polarizations and cell volumes for all stable  $\text{Sn}_2\text{P}_2\text{S}_{6(1-x)}\text{Se}_{6x}$  configurations as a function of Se concentration. Remarkably, after alloying FE  $\text{Sn}_2\text{P}_2\text{S}_6$  with another paraelectric compound, the overall FE polarizations for resulting  $\text{Sn}_2\text{P}_2\text{S}_{6(1-x)}\text{Se}_{6x}$  solid solutions are not significantly reduced but even slightly enhanced over the single-phase FE  $\text{Sn}_2\text{P}_2\text{S}_6$ . As Se anion has a large ionic radius than that of S, replacing S by Se can lead to the expansion of the cell volume of  $\text{Sn}_2\text{P}_2\text{S}_{6(1-x)}\text{Se}_{6x}$  over  $\text{Sn}_2\text{P}_2\text{S}_6$  (Figure 3c). Volume expansion-induced negative pressure effect is responsible for polarization enhancement in  $\text{Sn}_2\text{P}_2\text{S}_{6(1-x)}\text{Se}_{6x}$ . In fact, negative pressure effect has been successfully applied to improve the ferroelectricity and piezoelectric responses of FE perovskites.<sup>55,56</sup> Therefore, under the low Se concentration

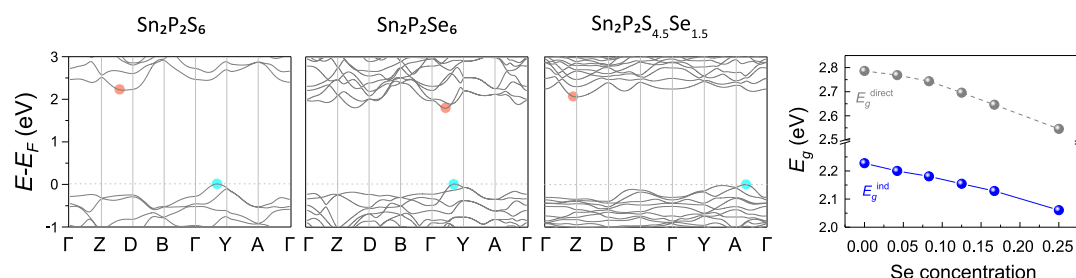


**Figure 4.** Calculated band structures of single-phase  $\text{Sn}_2\text{P}_2\text{S}_6$ ,  $\text{Sn}_2\text{P}_2\text{Se}_6$ , and  $\text{Sn}_2\text{P}_2\text{S}_{4.5}\text{Se}_{1.5}$  configuration (Se concentration  $x = 25\%$ ) as well as variation of indirect and direct energy band gaps with respect to Se concentration for most stable  $\text{Sn}_2\text{P}_2\text{S}_{6(1-x)}\text{Se}_{6x}$  configurations. Calculated energy gaps for other stable  $\text{Sn}_2\text{P}_2\text{S}_{6(1-x)}\text{Se}_{6x}$  configurations are tabulated in Figure S2. Positions for VBM and CBM in band structure plots are marked as blue and red circles, respectively.

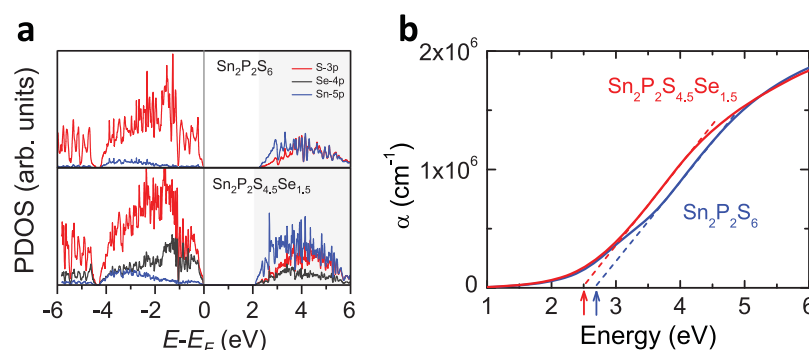


**Figure 5.** (a) PDOS and (b) optical absorption coefficient ( $\alpha(\omega)$ ) for FE  $\text{Sn}_2\text{P}_2\text{S}_6$  and  $\text{Sn}_2\text{P}_2\text{S}_{4.5}\text{Se}_{1.5}$  configuration calculated using HSE hybrid functional. The conduction states in PDOS are marked as gray areas. Dashed lines in (b) are extrapolated to identify the effective optical absorption edges (indicated by the arrows) for the two compounds.

range ( $x \leq 25\%$ ),  $\text{Sn}_2\text{P}_2\text{S}_{6(1-x)}\text{Se}_{6x}$  solid solutions with periodic and commensurate structural phases can exhibit the FE polarizations comparable or even superior to single-phase  $\text{Sn}_2\text{P}_2\text{S}_6$ .

**Electronic Structures and Optical Absorption Properties.** Unlike the traditional FE perovskite oxides (e.g.,  $\text{BaTiO}_3$ ), which are wide-gap insulators unsuitable for PV applications,  $\text{Sn}_2\text{P}_2\text{S}_6$  is a rare FE sulfide with semiconducting band gap. To evaluate the performance of  $\text{Sn}_2\text{P}_2\text{S}_6$  and  $\text{Sn}_2\text{P}_2\text{S}_{6(1-x)}\text{Se}_{6x}$  solid solutions as FE-PV materials, the electronic and optical absorption properties of these chalcogenide compounds will be investigated in this subsection.

We first compute the electronic structures for single-phase FE  $\text{Sn}_2\text{P}_2\text{S}_6$  and paraelectric  $\text{Sn}_2\text{P}_2\text{Se}_6$  using HSE hybrid functional. Figure 4 displays our calculated band structures for the two compounds. Both  $\text{Sn}_2\text{P}_2\text{S}_6$  and  $\text{Sn}_2\text{P}_2\text{Se}_6$  are semiconductors with indirect band gaps. Their valence band maximum (VBM) and conduction band minimum (CBM) are located along the high-symmetry directions of the Brillouin zone, away from  $\Gamma$  point. The direct energy band gaps measured at  $\Gamma$  point for both  $\text{Sn}_2\text{P}_2\text{S}_6$  and  $\text{Sn}_2\text{P}_2\text{Se}_6$  are predicted to be larger than their indirect  $E_g$ . More importantly, HSE calculated indirect  $E_g$  for  $\text{Sn}_2\text{P}_2\text{S}_6$  is very close to the experimental values (Table 1). Therefore, HSE functional can accurately predict electronic structures, especially energy band gaps for phosphorus chalcogenide compounds, which is crucial for precise simulation of their optical absorption properties.

Our calculations predict that single-phase  $\text{Sn}_2\text{P}_2\text{S}_6$  has a smaller  $E_g$  than  $\text{Sn}_2\text{P}_2\text{Se}_6$  (indirect  $E_g$ : 1.80 vs 2.23 eV, direct  $E_g$ : 2.22 vs 2.79 eV). The decrease in energy band gap with respect to Se doping is therefore expected in  $\text{Sn}_2\text{P}_2\text{S}_{6(1-x)}\text{Se}_{6x}$  solid

solutions. After performing electronic structure calculations for most stable  $\text{Sn}_2\text{P}_2\text{S}_{6(1-x)}\text{Se}_{6x}$  configurations under different Se concentrations using HSE functional, the monotonic decrease in both direct and indirect  $E_g$  with respect to Se concentration is found in  $\text{Sn}_2\text{P}_2\text{S}_{6(1-x)}\text{Se}_{6x}$  configurations (Figure 4). Typically, after 25% Se doping,  $\text{Sn}_2\text{P}_2\text{S}_{4.5}\text{Se}_{1.5}$  configuration is predicted as an indirect band gap semiconductor (band structure shown in Figure 4), with a direct band gap at  $\Gamma$  point of 2.55 eV, which is smaller than that of  $\text{BiFeO}_3$  (direct  $E_g = 2.67$  eV),<sup>14</sup> a FE material widely used for PV applications. Moreover, after parabolic fitting of energy bands around CBM and VBM,  $\text{Sn}_2\text{P}_2\text{S}_{4.5}\text{Se}_{1.5}$  configuration is predicted to have carrier effective mass ( $m_e^* = 0.42$ ,  $m_h^* = 0.74m_0$ ) close to single-phase  $\text{Sn}_2\text{P}_2\text{S}_6$  ( $m_e^* = 0.58$ ,  $m_h^* = 0.65m_0$ ), indicating that Se substitution will not significantly affect the overall effective mass and carrier mobility of the parent  $\text{Sn}_2\text{P}_2\text{S}_6$  system.

To obtain a better understanding of Se doping induced band gap reduction in  $\text{Sn}_2\text{P}_2\text{S}_{6(1-x)}\text{Se}_{6x}$  configurations, we calculate partial density of states (PDOS) for single-phase  $\text{Sn}_2\text{P}_2\text{S}_6$  and  $\text{Sn}_2\text{P}_2\text{S}_{4.5}\text{Se}_{1.5}$  configuration using HSE functional. Consistent with experimental X-ray photoelectron valence-band spectrum,<sup>28</sup> majority of valence states for FE  $\text{Sn}_2\text{P}_2\text{S}_6$  consist of S 3p orbitals, whereas conduction states are mainly composed of the hybridized Sn 5p and S 3p orbitals (Figure 5a). Similar to FE perovskite oxides, such as  $\text{PbTiO}_3$  and  $\text{BaTiO}_3$ ,<sup>57</sup> the hybridization between cation and anion orbitals should be crucial for ferroelectricity in  $\text{Sn}_2\text{P}_2\text{S}_6$ . After Se doping, besides Sn 5p and S 3p hybridization, there also exists the pronounced hybridization between Sn 5p and Se 4p orbitals throughout both valence and conduction states in  $\text{Sn}_2\text{P}_2\text{S}_{4.5}\text{Se}_{1.5}$  configuration. Moreover, Se substitution does not introduce any gap states into the system. As a result, the energy band gaps for

$\text{Sn}_2\text{P}_2\text{S}_6$  and  $\text{Sn}_2\text{P}_2\text{S}_{4.5}\text{Se}_{1.5}$  compounds are primarily determined by the orbital hybridization between Sn cation and S/Se anions. As atomic energy level of Se 4p orbital is lower than that of S 3p,<sup>34</sup> hybridization between Sn 5p and Se 4p orbitals can generate a small band gap in selenide. Moreover, as Se concentration increases, the shorter Sn–Se bond (Figure S4) enables larger amount of hybridization (orbital overlap) between Sn 5p and Se 4p, which can lead to a smaller  $E_g$ . Therefore, substitution-induced Sn–Se bond change is responsible for band gap reduction with respect to Se concentration in  $\text{Sn}_2\text{P}_2\text{S}_{6(1-x)}\text{Se}_{6x}$  configurations.

The reduced band gap of  $\text{Sn}_2\text{P}_2\text{S}_{4.5}\text{Se}_{1.5}$  configuration can lead to the improved visible-light absorption of  $\text{Sn}_2\text{P}_2\text{S}_{4.5}\text{Se}_{1.5}$  over  $\text{Sn}_2\text{P}_2\text{S}_6$ . In order to evaluate the optical absorption properties of the two compounds, their optical absorption coefficients  $\alpha(\omega)$  are simulated.  $\alpha(\omega)$  can be obtained by calculating the frequency-dependent dielectric function  $\varepsilon(\omega)$  based on the independent particle approximation implemented in VASP (computational details can be found in ref 21). More than 140 empty bands are included for dielectric function calculations, so that our simulated  $\varepsilon(\omega)$  are well converged as they satisfy the  $f$ -sum rule (formulated as:  $-\int_0^\infty \text{Im}(1/\varepsilon(\omega))1/\omega \, d\omega \approx \pi/2$ ).

Figure 5b displays our simulated optical absorption coefficients  $\alpha(\omega)$  for  $\text{Sn}_2\text{P}_2\text{S}_6$  and  $\text{Sn}_2\text{P}_2\text{S}_{4.5}\text{Se}_{1.5}$ . Owing to their indirect band gaps, optical absorption coefficients for both  $\text{Sn}_2\text{P}_2\text{S}_6$  and  $\text{Sn}_2\text{P}_2\text{S}_{4.5}\text{Se}_{1.5}$  around the energy close to their indirect  $E_g$  are quite weak, as  $\alpha(\omega)$  near the indirect  $E_g$  shows quadratic dependence on the photon energy ( $\alpha \propto (\hbar\nu - E_g)^2$ ).<sup>58</sup> As a result,  $\text{Sn}_2\text{P}_2\text{S}_6$  and  $\text{Sn}_2\text{P}_2\text{S}_{4.5}\text{Se}_{1.5}$  can only effectively absorb the incident light whose photon energy is above their optical absorption edges. We identify the effective optical absorption edges for two compounds after the extrapolation of the simulated  $\alpha(\omega)$  (shown in Figure 5b). Our simulation predicts an optical absorption edge of 2.69 eV for single-phase  $\text{Sn}_2\text{P}_2\text{S}_6$ , whereas experimental measured values range from 2.40 to 2.70 eV.<sup>59–61</sup> After Se doping, optical absorption edge of  $\text{Sn}_2\text{P}_2\text{S}_{4.5}\text{Se}_{1.5}$  configuration can be further reduced up to 2.51 eV. Accordingly,  $\text{Sn}_2\text{P}_2\text{S}_{4.5}\text{Se}_{1.5}$  is able to effectively absorb a larger portion of the visible spectrum. As a stoichiometric compound,  $\text{Sn}_2\text{P}_2\text{S}_{4.5}\text{Se}_{1.5}$  solid solution simultaneously shows the FE polarization and optical absorption properties more superior to those of single-phase  $\text{Sn}_2\text{P}_2\text{S}_6$ . Therefore, the improved PV performance is expected in FE-PV device based on Se-doped  $\text{Sn}_2\text{P}_2\text{S}_6$  compounds.

## CONCLUSIONS

In summary, we perform first-principles calculations to investigate the structural, FE, electronic, and optical absorption properties of non-perovskite phosphorus chalcogenides  $\text{Sn}_2\text{P}_2\text{S}_6$ ,  $\text{Sn}_2\text{P}_2\text{Se}_6$  and their solid solutions  $\text{Sn}_2\text{P}_2\text{S}_{6(1-x)}\text{Se}_{6x}$  ( $x \leq 25\%$ ). Our calculations reveal that, unlike FE  $\text{Sn}_2\text{P}_2\text{S}_6$ , single-phase selenide  $\text{Sn}_2\text{P}_2\text{Se}_6$  crystallizes in a paraelectric phase, without any detectable FE polarization. After alloy FE  $\text{Sn}_2\text{P}_2\text{S}_6$  with paraelectric selenide, the resulting  $\text{Sn}_2\text{P}_2\text{S}_{6(1-x)}\text{Se}_{6x}$  solid solutions with low Se concentration ( $x \leq 25\%$ ) still exhibit the FE polarization comparable with the parent  $\text{Sn}_2\text{P}_2\text{S}_6$ . Moreover, Se substitution-induced effective “band gap engineering” is achieved in  $\text{Sn}_2\text{P}_2\text{S}_{6(1-x)}\text{Se}_{6x}$  systems. Especially,  $\text{Sn}_2\text{P}_2\text{S}_{4.5}\text{Se}_{1.5}$  compound with Se concentration of 25% has a smaller optical absorption edge than single phase  $\text{Sn}_2\text{P}_2\text{S}_6$ , enabling the more effective absorption of the visible light. On the basis of the spectrally more suitable energy band

gap and stable FE polarization, we propose that FE  $\text{Sn}_2\text{P}_2\text{S}_{4.5}\text{Se}_{1.5}$  compound can exhibit improved PV performance than single-phase  $\text{Sn}_2\text{P}_2\text{S}_6$ . As  $\text{Sn}_2\text{P}_2\text{S}_{6(1-x)}\text{Se}_{6x}$  solid solutions are experimentally synthesized compounds, our work will further motivate the future experimental exploration of their FE-PV properties.

## ASSOCIATED CONTENT

### Supporting Information

The Supporting Information is available free of charge on the ACS Publications website at DOI: 10.1021/acs.jpcc.8b08402.

The calculated crystallographic structures for single-phase  $\text{Sn}_2\text{P}_2\text{S}_6$  and  $\text{Sn}_2\text{P}_2\text{Se}_6$ , atomic structures for all stable  $\text{Sn}_2\text{P}_2\text{S}_{6(1-x)}\text{Se}_{6x}$  configurations, phonon spectrum of  $\text{Sn}_2\text{P}_2\text{S}_{4.5}\text{Se}_{1.5}$  configuration and variation of Sn–Se bond length in  $\text{Sn}_2\text{P}_2\text{S}_{6(1-x)}\text{Se}_{6x}$  with respect to Se concentration (PDF)

## AUTHOR INFORMATION

### Corresponding Author

\*E-mail: gougayang@mail.xjtu.edu.cn.

### ORCID

Gaoyang Gou: 0000-0003-1485-8115

### Notes

The authors declare no competing financial interest.

## ACKNOWLEDGMENTS

Authors acknowledge the funding from National Science Foundation of China under contract nos. 11574244, 51320105014 and 51621063, State Key Laboratory for Mechanical Behavior of Materials; and computational support from National Supercomputer Centre (NSCC) in Tianjin.

## REFERENCES

- (1) Fan, Z.; Sun, K.; Wang, J. Perovskites for Photovoltaics: A Combined Review of Organic-Inorganic Halide Perovskites and Ferroelectric Oxide Perovskites. *J. Mater. Chem. A* **2015**, *3*, 18809–18828.
- (2) Butler, K. T.; Frost, J. M.; Walsh, A. Ferroelectric Materials for Solar Energy Conversion: Photoferroics Revisited. *Energy Environ. Sci.* **2015**, *8*, 838–848.
- (3) Yuan, Y.; Xiao, Z.; Yang, B.; Huang, J. Arising Applications of Ferroelectric Materials in Photovoltaic Devices. *J. Mater. Chem. A* **2014**, *2*, 6027–6041.
- (4) Seidel, J.; Eng, L. M. Shedding Light on Nanoscale Ferroelectrics. *Curr. Appl. Phys.* **2014**, *14*, 1083–1091.
- (5) Choi, T.; Lee, S.; Choi, Y. J.; Kiryukhin, V.; Cheong, S.-W. Switchable Ferroelectric Diode and Photovoltaic Effect in  $\text{BiFeO}_3$ . *Science* **2009**, *324*, 63–66.
- (6) Guo, R.; You, L.; Zhou, Y.; Lim, Z. S.; Zou, X.; Chen, L.; Ramesh, R.; Wang, J. Non-Volatile Memory Based on the Ferroelectric Photovoltaic Effect. *Nat. Commun.* **2013**, *4*, 1990.
- (7) Yang, S. Y.; Seidel, J.; Byrnes, S. J.; Shafer, P.; Yang, C.-H.; Rossell, M. D.; Yu, P.; Chu, Y.-H.; Scott, J. F.; Ager, J. W., III; Martin, L. W.; Ramesh, R. Above-Bandgap Voltages from Ferroelectric Photovoltaic Devices. *Nat. Nanotechnol.* **2010**, *5*, 143–147.
- (8) Seidel, J.; Fu, D.; Yang, S.-Y.; Alarcón-Lladó, E.; Wu, J.; Ramesh, R.; Ager, J. W. Efficient Photovoltaic Current Generation at Ferroelectric Domain Walls. *Phys. Rev. Lett.* **2011**, *107*, 126805.
- (9) Ji, W.; Yao, K.; Liang, Y. C. Bulk Photovoltaic Effect at Visible Wavelength in Epitaxial Ferroelectric  $\text{BiFeO}_3$  Thin Films. *Adv. Mater.* **2010**, *22*, 1763–1766.
- (10) Zhang, L.; Chen, J.; Cao, J.; He, D.; Xing, X. Large Resistive Switching and Switchable Photovoltaic Response in Ferroelectric



Doped BiFeO<sub>3</sub>-based Thin Films by Chemical Solution Deposition. *J. Mater. Chem. C* **2015**, *3*, 4706–4712.

(11) Nechache, R.; Harnagea, C.; Li, S.; Cardenas, L.; Huang, W.; Chakrabarty, J.; Rosei, F. Bandgap Tuning of Multiferroic Oxide Solar Cells. *Nat. Photonics* **2014**, *9*, 61–67.

(12) Quattropiani, A.; Stoeffler, D.; Fix, T.; Schmerber, G.; Lenertz, M.; Versini, G.; Rehspringer, J. L.; Slaoui, A.; Dinia, A.; Colis, S. Band-Gap Tuning in Ferroelectric Bi<sub>2</sub>FeCrO<sub>6</sub> Double Perovskite Thin Films. *J. Phys. Chem. C* **2018**, *122*, 1070–1077.

(13) Bennett, J. W.; Rabe, K. M. Integration of First-Principles Methods and Crystallographic Database Searches for New Ferroelectrics: Strategies and Explorations. *J. Solid State Chem.* **2012**, *195*, 21–31.

(14) Yang, S. Y.; Martin, L. W.; Byrnes, S. J.; Conry, T. E.; Basu, S. R.; Paran, D.; Reichertz, L.; Ihlefeld, J.; Adamo, C.; Melville, A.; et al. Photovoltaic Effects in BiFeO<sub>3</sub>. *Appl. Phys. Lett.* **2009**, *95*, 062909.

(15) Grinberg, I.; West, D. V.; Torres, M.; Gou, G.; Stein, D. M.; Wu, L.; Chen, G.; Gallo, E. M.; Akbashev, A. R.; Davies, P. K.; Spanier, J. E.; Rappe, A. M. Perovskite Oxides for Visible-Light-Absorbing Ferroelectric and Photovoltaic Materials. *Nature* **2013**, *503*, 509–512.

(16) Choi, W. S.; Chisholm, M. F.; Singh, D. J.; Choi, T.; Jellison, G. E., Jr; Lee, H. N. Wide Bandgap Tunability in Complex Transition Metal Oxides by Site-Specific Substitution. *Nat. Commun.* **2012**, *3*, 689.

(17) Xu, X. S.; Ihlefeld, J. F.; Lee, J. H.; Ezekoye, O. K.; Vlahos, E.; Ramesh, R.; Gopalan, V.; Pan, X. Q.; Schlom, D. G.; Musfeldt, J. L. Tunable Band Gap in Bi(Fe<sub>1-x</sub>Mn<sub>x</sub>)O<sub>3</sub> Films. *Appl. Phys. Lett.* **2010**, *96*, 192901.

(18) Berger, R. F.; Neaton, J. B. Computational Design of Low-Band-Gap Double Perovskites. *Phys. Rev. B: Condens. Matter Mater. Phys.* **2012**, *86*, 165211.

(19) Gou, G. Y.; Bennett, J. W.; Takenaka, H.; Rappe, A. M. Post Density Functional Theoretical Studies of Highly Polar Semiconductive Pb(Ti<sub>1-x</sub>Ni<sub>x</sub>)O<sub>3-x</sub> Solid Solutions: Effects of Cation Arrangement on Band Gap. *Phys. Rev. B: Condens. Matter Mater. Phys.* **2011**, *83*, 205115.

(20) Bennett, J. W.; Grinberg, I.; Rappe, A. M. New Highly Polar Semiconductor Ferroelectrics through d<sup>8</sup> Cation-O Vacancy Substitution into PbTiO<sub>3</sub>: A Theoretical Study. *J. Am. Chem. Soc.* **2008**, *130*, 17409–17412.

(21) Wang, H.; Gou, G.; Li, J. Ruddlesden-Popper Perovskite Sulfides A<sub>3</sub>B<sub>2</sub>S<sub>7</sub>: A New Family of Ferroelectric Photovoltaic Materials for the Visible Spectrum. *Nano Energy* **2016**, *22*, 507–513.

(22) Moriya, K.; Kuniyoshi, H.; Tashita, K.; Ozaki, Y.; Yano, S.; Matsuo, T. Ferroelectric Phase Transitions in Sn<sub>2</sub>P<sub>2</sub>S<sub>6</sub> and Sn<sub>2</sub>P<sub>2</sub>Se<sub>6</sub> Crystals. *J. Phys. Soc. Jpn.* **1998**, *67*, 3505–3511.

(23) Carpentier, C. D.; Nitsche, R. Vapour Growth and Crystal Data of the Thio(seleno)-Hypodiphosphates Sn<sub>2</sub>P<sub>2</sub>S<sub>6</sub>, Sn<sub>2</sub>P<sub>2</sub>Se<sub>6</sub>, Pb<sub>2</sub>P<sub>2</sub>Se<sub>6</sub> and Their Mixed Crystals. *Mater. Res. Bull.* **1974**, *9*, 401–410.

(24) Cho, Y. W.; Choi, S. K.; Vysotskii, Y. M. Photovoltaic Effect of Sn<sub>2</sub>P<sub>2</sub>S<sub>6</sub> Ferroelectric Crystal and Ceramics. *J. Mater. Res.* **2001**, *16*, 3317–3322.

(25) Ovsyannikov, S. V.; Gou, H.; Morozova, N. V.; Tyagur, I.; Tyagur, Y.; Shchennikov, V. V. Raman Spectroscopy of Ferroelectric Sn<sub>2</sub>P<sub>2</sub>S<sub>6</sub> under High Pressure up to 40 GPa: Phase Transitions and Metallization. *J. Appl. Phys.* **2013**, *113*, 013511.

(26) Studenyak, I. P.; Mitrovic, V. V.; Kovacs, G. S.; Mykajlo, O. A.; Gurzan, M. I.; Vysotskii, Y. M. Temperature Variation of Optical Absorption Edge in Sn<sub>2</sub>P<sub>2</sub>S<sub>6</sub> and SnP<sub>2</sub>S<sub>6</sub> Crystals. *Ferroelectrics* **2001**, *254*, 295–310.

(27) Rong, Y.; Li, M.; Chen, J.; Zhou, M.; Lin, K.; Hu, L.; Yuan, W.; Duan, W.; Deng, J.; Xing, X. Large Negative Thermal Expansion in Non-Perovskite Lead-Free Ferroelectric Sn<sub>2</sub>P<sub>2</sub>S<sub>6</sub>. *Phys. Chem. Chem. Phys.* **2016**, *18*, 6247–6251.

(28) Kuepper, K.; Schneider, B.; Caciuc, V.; Neumann, M.; Postnikov, A. V.; Ruediger, A.; Grabar, A. A.; Vysotskii, Y. M. Electronic Structure of Sn<sub>2</sub>P<sub>2</sub>S<sub>6</sub>. *Phys. Rev. B: Condens. Matter Mater. Phys.* **2003**, *67*, 115101.

(29) Tyagur, Y. Spontaneous Polarization in Sn<sub>2</sub>P<sub>2</sub>S<sub>6</sub> Ferroelectric Single Crystals. *Ferroelectrics* **2006**, *345*, 91–101.

(30) Li, Y.; Singh, D. J. Properties of the Ferroelectric Visible Light Absorbing Semiconductors: Sn<sub>2</sub>P<sub>2</sub>S<sub>6</sub> and Sn<sub>2</sub>P<sub>2</sub>Se<sub>6</sub>. *Phys. Rev. Mater.* **2017**, *1*, 075402.

(31) Eijt, S. W. H.; Currat, R.; Lorenzo, J. E.; Saint-Grégoire, P.; Katano, S.; Janssen, T.; Hennion, B.; Vysotskii, Y. M. Soft Modes and Phonon Interactions in Sn<sub>2</sub>P<sub>2</sub>Se<sub>6</sub> Studied by Means of Neutron Scattering. *J. Phys.: Condens. Matter* **1998**, *10*, 4811–4844.

(32) Brehm, J. A.; Takenaka, H.; Lee, C.-W.; Grinberg, I.; Bennett, J. W.; Schoenberg, M. R.; Rappe, A. M. Density Functional Theory Study of Hypothetical PbTiO<sub>3</sub>-based Oxyulfides. *Phys. Rev. B: Condens. Matter Mater. Phys.* **2014**, *89*, 195202.

(33) Brehm, J. A.; Bennett, J. W.; Schoenberg, M. R.; Grinberg, I.; Rappe, A. M. The Structural Diversity of AB<sub>3</sub> Compounds with d<sup>0</sup> Electronic Configuration for the B-cation. *J. Chem. Phys.* **2014**, *140*, 224703.

(34) Sun, Y.-Y.; Agiorgousis, M. L.; Zhang, P.; Zhang, S. Chalcogenide Perovskites for Photovoltaics. *Nano Lett.* **2015**, *15*, 581–585.

(35) Padlyak, B.; Vlokh, R.; Grabar, A.; Vysotskii, Y.; Dmitruk, I.; Ryba-Romanowski, W.; Lisiecki, R. Luminescence Properties of Sn<sub>2</sub>P<sub>2</sub>Se<sub>6</sub> Crystals. *Opt. Mater.* **2009**, *31*, 1831–1834.

(36) Rushchanskii, K. Z.; Molnar, A.; Bilanych, R.; Yevych, R.; Kohutych, A.; Vysotskii, Y. M.; Samulionis, V.; Banys, J. Observation of Nonequilibrium Behavior near the Lifshitz Point in Ferroelectrics with Incommensurate Phase. *Phys. Rev. B: Condens. Matter Mater. Phys.* **2016**, *93*, 014101.

(37) Kresse, G.; Furthmüller, J. Efficient Iterative Schemes for *ab initio* Total-Energy Calculations Using a Plane-Wave Basis Set. *Phys. Rev. B: Condens. Matter Mater. Phys.* **1996**, *54*, 11169–11186.

(38) Kresse, G.; Joubert, D. From Ultrasoft Pseudopotentials to the Projector Augmented-Wave Method. *Phys. Rev. B: Condens. Matter Mater. Phys.* **1999**, *59*, 1758–1775.

(39) Blöchl, P. E. Projector Augmented-Wave Method. *Phys. Rev. B: Condens. Matter Mater. Phys.* **1994**, *50*, 17953–17979.

(40) Perdew, J. P.; Ruzsinszky, A.; Csonka, G. I.; Vydrov, O. A.; Scuseria, G. E.; Constantin, L. A.; Zhou, X.; Burke, K. Restoring the Density-Gradient Expansion for Exchange in Solids and Surfaces. *Phys. Rev. Lett.* **2008**, *100*, 136406.

(41) Wahl, R.; Vogtenhuber, D.; Kresse, G. SrTiO<sub>3</sub> and BaTiO<sub>3</sub> Revisited using the Projector Augmented Wave Method: Performance of Hybrid and Semilocal Functionals. *Phys. Rev. B: Condens. Matter Mater. Phys.* **2008**, *78*, 104116.

(42) Monkhorst, H. J.; Pack, J. D. Special Points for Brillouin-Zone Integrations. *Phys. Rev. B: Solid State* **1976**, *13*, 5188–5192.

(43) Heyd, J.; Scuseria, G. E.; Ernzerhof, M. Hybrid Functionals Based on a Screened Coulomb Potential. *J. Chem. Phys.* **2003**, *118*, 8207–8215.

(44) Baroni, S.; de Gironcoli, S.; Dal Corso, A.; Giannozzi, P. Phonons and Related Crystal Properties from Density-Functional Perturbation Theory. *Rev. Mod. Phys.* **2001**, *73*, 515–562.

(45) Gonze, X. Adiabatic Density-Functional Perturbation Theory. *Phys. Rev. A: At., Mol., Opt. Phys.* **1995**, *52*, 1096–1114.

(46) King-Smith, R. D.; Vanderbilt, D. Theory of Polarization of Crystalline Solids. *Phys. Rev. B: Condens. Matter Mater. Phys.* **1993**, *47*, 1651–1654.

(47) Rushchanskii, K. Z.; Vysotskii, Y. M.; Strauch, D. Ferroelectricity, Nonlinear Dynamics, and Relaxation Effects in Monoclinic Sn<sub>2</sub>P<sub>2</sub>S<sub>6</sub>. *Phys. Rev. Lett.* **2007**, *99*, 207601.

(48) Dittmar, G.; Schäfer, H. The Crystal Structure of Sn<sub>2</sub>P<sub>2</sub>S<sub>6</sub>. *Z. Naturforsch. B* **1974**, *29*, 312–317.

(49) Gamerny, R. V.; Gnatenko, Y. P.; Bukivskij, P. M.; Skubenko, P. A.; Slivka, V. Y. Optical and Photoelectric Spectroscopy of Photorefractive Sn<sub>2</sub>P<sub>2</sub>S<sub>6</sub> Crystals. *J. Phys.: Condens. Matter* **2006**, *18*, 5323–5331.

(50) Scott, B.; Pressprich, M.; Willet, R. D.; Cleary, D. A. High Temperature Crystal Structure and DSC of Sn<sub>2</sub>P<sub>2</sub>S<sub>6</sub>. *J. Solid State Chem.* **1992**, *96*, 294–300.

- (51) Israël, R.; De Gelder, R.; Smits, J. M. M.; Beurskens, P. T.; Eijt, S. W. H.; Rasing, T.; van Kempen, H.; Maior, M. M.; Motrija, S. F. Crystal Structures of Di-Tin-Hexa(seleno)hypodiphosphate,  $\text{Sn}_2\text{P}_2\text{Se}_6$ , in the Ferroelectric and Paraelectric Phase. *Z. Kristallogr.* **1998**, *213*, 34–41.
- (52) Abrahams, S. C.; Kurtz, S. K.; Jamieson, P. B. Atomic Displacement Relationship to Curie Temperature and Spontaneous Polarization in Displacive Ferroelectrics. *Phys. Rev.* **1968**, *172*, 551–553.
- (53) Zhang, J.; Gou, G.; Pan, B. Study of Phase Stability and Hydride Diffusion Mechanism of  $\text{BaTiO}_3$  Oxyhydride from First-Principles. *J. Phys. Chem. C* **2014**, *118*, 17254–17259.
- (54) Slivka, A. G.; Gerzanich, E. I.; Guranich, P. P.; Shusta, V. S. Phase  $p$ ,  $T$ ,  $x$ -Diagram and Peculiarities of Physical Properties of  $\text{Sn}_2\text{P}_2(\text{Se}_x\text{S}_{1-x})_6$  Ferroelectric Crystals near Lifshitz Point. *Ferroelectrics* **1990**, *103*, 71–82.
- (55) Tinte, S.; Rabe, K. M.; Vanderbilt, D. Anomalous Enhancement of Tetragonality in  $\text{PbTiO}_3$  Induced by Negative Pressure. *Phys. Rev. B: Condens. Matter Mater. Phys.* **2003**, *68*, 144105.
- (56) Gou, G.; Shi, J. Piezoelectricity Enhancement in Dion-Jacobson  $\text{RbBiNb}_2\text{O}_7$  via Negative Pressure. *Europhys. Lett.* **2014**, *108*, 67006.
- (57) Cohen, R. E. Origin of Ferroelectricity in Perovskite Oxides. *Nature* **1992**, *358*, 136–138.
- (58) Gou, G.; Charles, N.; Shi, J.; Rondinelli, J. M. A-Site Ordered Double Perovskite  $\text{CaMnTi}_2\text{O}_6$  as a Multifunctional Piezoelectric and Ferroelectric-Photovoltaic Material. *Inorg. Chem.* **2017**, *56*, 11854–11861.
- (59) Gerzanich, E. I. Optical Properties of  $\text{A}_2\text{B}_2\text{C}_6$  Ferroelectrics-Semiconductors: the Effect of Temperature and Hydrostatic Pressure. *Ukr. J. Phys. Opt.* **2008**, *9*, 129–163.
- (60) Ruediger, A.; Schirmer, O.; Odoulov, S.; Shumelyuk, A.; Grabar, A. Studies of Light-Induced Charge Transfer in  $\text{Sn}_2\text{P}_2\text{S}_6$  by Combined EPR/Optical Absorption Spectroscopy. *Opt. Mater.* **2001**, *18*, 123–125.
- (61) Studenyak, I. P.; Mitrovicij, V. V.; Kovacs, G. S.; Mykajlo, O. A.; Gurzan, M. I.; Vysochanskii, Y. M. Temperature Variation of Optical Absorption Edge in  $\text{Sn}_2\text{P}_2\text{S}_6$  and  $\text{SnP}_2\text{S}_6$  Crystals. *Ferroelectrics* **2001**, *254*, 295–310.